Janus Gold Nanoparticles from Nanodroplets of Alkyl Thiols: A Molecular Dynamics Study

Debdip Bhandary,[†] Vasumathi Valechi,[‡] Maria Natália D. S. Cordeiro,[‡] and Jayant K. Singh*,[†]

[†]Department of Chemical Engineering, Indian Institute of Technology Kanpur, Kanpur, Uttar Pradesh 208016, India
[‡]LAQV@REQUIMTE/Department of Chemistry and Biochemistry, Faculty of Sciences, University of Porto, 4169-007 Porto, Portugal

Ⓢ Supporting Information

ABSTRACT: Janus particles provide an asymmetry in structure, which can impart diverse functionalities leading to immense importance in various applications, ranging from targeted delivery to interfacial phenomena, including catalysis, electronics, and optics. In this work, we present results of a molecular dynamics study of the growth mechanism of coating on gold nanoparticles (AuNPs) from droplets of n-alkyl thiols with different chain lengths (C5 and C11) and terminal groups (CH$_3$ and COOH). The effect of chain lengths and functional groups on the formation of a monolayer of alkyl thiols on AuNPs is investigated. A two-step mechanism, initiated by the binding of the droplet to the nanoparticle surface with a time constant on the order of ~1 ns, followed by the diffusion-driven growth with a larger time constant (on the order of 100 ns), is shown to capture the growth dynamics of the monolayer. It is observed that the time required for complete wetting increases with an increase in the chain length. Moreover, the monolayer formation is slowed down in the presence of carboxyl groups because of strong hydrogen bonding. The kinetics of the n-alkyl thiols coating on the nanoparticles is found to be independent of the droplet size but carboxyl-terminated thiols spread more with increasing droplet size. Furthermore, different time constants for different chains and functional groups yield Janus coating when two droplets of alkyl thiols with different terminal groups are allowed to form monolayers on the nanoparticle. The Janus balance (β) for different combinations of alkyl thiols and nanoparticle sizes varies in the range of 0.42−0.71.
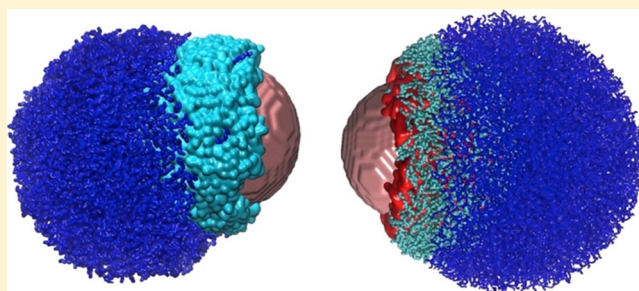
I. INTRODUCTION

Janus particles (JPs) have gained significant attention in the area of targeted delivery, catalysis, biomedical applications, electronics, and optical applications because of their broken symmetry. Furthermore, different physical and chemical properties of JPs promote the generation of asymmetric interfaces that open the possibilities for unique ways of interfacial mesostructuration.[1,2] Depending upon the nature and shape of the JPs, their behavior changes.[1] For instance, Xu et al.[3] studied the behavior of Janus rods in phase-separated polymers. The authors showed that the nanorod orientation parallel to the interface of two polymers provides a simple route to generate percolated nanowires spatially distributed along the phase interface, which can control the structural evolution of polymer nanocomposites. Different architectures of JPs within a copolymer assembly lead to the formation of different assembled structures at the interface, and regulation of JPs can alter the interfacial properties and structural evolution.[4] For example, Discher and co-workers[5] created synthetic Janus vesicles based on block copolymers for drug delivery applications in biomedicine.

Peanut-shaped JP vesicles are used to gain fundamental insights into lipid composition-based heterogeneity and membrane-mediated interactions.[6,7] The behavior of assemblies of JPs changes depending upon the optical and electrical response of the different faces of the JPs.[8,9] The catalytic activity at the broken symmetry can be used for the propulsion of nanoparticles in biomedical devices.[10,11] Whereas preferential binding of biomolecules on one face of the JPs can help in the detection technology,[12,13] magnetic JPs are applicable in therapeutics.[14]

Gold-based JPs have so far been the most actively investigated, in particular, because of their robustness when covered with thiol-type ligands, combined with multiple applications of gold nanoparticles (AuNPs) in areas such as drug delivery, catalysis, electrochemical charging, and molecular recognition, to name just a few.[15] Moreover, the formation of self-assembled monolayers (SAMs) on gold is an easy way to prepare functionalized nanoparticles, and hence the stability and solubility of the particles can be easily altered.[15−17]

Several experimental techniques such as one-sided gold deposition,[18] colloidal crystallization,[19] microcontact printing,[20] electrified jetting,[21] microfluidics, Pickering-type emulsion, phase separation in confined volume, electrohydrodynamics,

and restricted nucleation and growth process[1,2] have been used to fabricate JPs. All of these experimental techniques for the fabrication of JPs fall under three main strategies: masking, phase separation, and self-assembly. Among these three methods, the masking method involves multiple steps, often relying on interfacial adhesion and partial modification of one part of a particle. Therefore, reducing the number of reaction steps greatly improves the sustainability of the reactions and scaling. Self-assembly and phase separation involves a single-step process for the JP formation; however, through self-assembly, JPs can be formed only when the size of AuNPs is below 3.5 nm.[22,23] Singh et al.[22] were the first to report that the Janus coating can be assembled through self-assembly, with a computational study, and they observed JPs for a 3.5 nm size of AuNPs, and above this size, stripe arrangement was observed. On the other hand, preparation of micro/nanoscale JPs using microfluidics techniques falls under phase separation methods and can lead to a good control in size and functionality. Moreover, such techniques show great promise in the manufacture of functional nanoparticles. Several authors[24−31] have reported the synthesis of JPs using microfluidics via the droplet-based side-by-side emulsification process pioneered by Nisisako et al.[24,25] One of the important criteria for this process/technique is that the viscosities of the liquids should closely match each other, and the interfacial tension of the liquids should be of the same order.[25] The flow rate of the fluid and its interfacial tension leads to proper distribution of the droplet sizes, thus enabling the Janus balance (JB) to be properly altered and controlled.[24] Along with polymer-based JPs, inorganic bimetallic nanoparticles and silica beads are widely synthesized using this technique. AuNPs with advanced optical and magnetic properties are usually set up with coemulsification because by doing so, they can easily respond to external electric and magnetic fields.

Although there are several experimental studies[23−31] on the fabrication of JPs using phase separation, computational studies are lacking, which explore the impact of the particle size, the length of thiol molecules, and the terminal group on JB.

In this work, using molecular dynamics (MD) simulations, we investigated the formation of Janus nanoparticles when droplets of different thiols are sprayed/dispersed in an extremely bad solvent (such as any gas, air, etc.) that contains AuNPs. Two droplets of immiscible/partially miscible thiols in the vicinity of AuNPs of different sizes lead to the formation of JPs with a different JB. The aim of the study is to understand the growth of a monolayer on nanoparticles in micro/nanofluidic processes, where the molecular interactions and rearrangement are the important parameters. Understanding the typical timeframe of the process, further modulation of other parameters could lead to a development in the nanofabrication of molecular devices. To the best of our knowledge, there are no studies on the adsorption of thiols on AuNPs from the nanodroplets of thiols, typically occurring in the micro/nanofluidics methods of formation of JPs. We also investigated the kinetics of adsorption of thiols with different tail groups on AuNPs with different sizes. In the next section, we describe the theoretical methods used, including potential models and simulation details. Our results are presented and discussed in section III, followed by the concluding remarks that are given in section IV.

II. MODEL AND METHODOLOGY

II.1. Model. To model the conformational energy of the alkyl thiol molecules, we have used the standard force field from the literature

$$U_{total} = U_{bonded} + U_{non-bonded} \tag{1}$$

Here, U_{bonded} represents the bonded interactions that arise from bond stretching (U_{str}), bond bending (U_{bend}), and torsion (U_{dihed})

$$U_{str} = \frac{1}{2}k_s(r - r_0); \qquad U_{bend} = \frac{1}{2}k_b(\theta - \theta_0) \tag{2}$$

$$U_{dihed} = \frac{1}{2}k_1[1 + \cos(\varphi)] + \frac{1}{2}k_2[1 - \cos(2\varphi)] + \frac{1}{2}k_3[1 + \cos(3\varphi)] + \frac{1}{2}k_4[1 - \cos(4\varphi)] \tag{3}$$

Here, r is the bond distance between two atoms, and r_0 is the equilibrium bond length. θ defines the angle between three atoms and θ_0 is the equilibrium angle. φ defines a dihedral angle of four atoms. k_s, k_b, k_1, k_2, k_3, and k_4 are constants.

Nonbonded interactions are modeled in terms of Lennard-Jones 12-6 (LJ-12-6) potential to calculate the nonbonded interaction between the atoms/particles along with the pairwise-additive Morse potential for the Au−S interaction. To model the chemisorption of Au−S, we used the scheme suggested by Ahn et al.,[32] which is applied for the interaction potential between Au and S, a swift shifting from LJ potential to Morse potential. The LJ pair potential is defined by

$$U_{LJ} = \sum_{ij} 4\varepsilon_{ij}\left[\left(\frac{\sigma_{ij}}{r_{ij}}\right)^{12} - \left(\frac{\sigma_{ij}}{r_{ij}}\right)^6\right] \tag{4}$$

where ε_{ij}, r_{ij}, and σ_{ij} are the potential well depth, the distance between two particles, and atomic diameter, respectively. For cross-interactions, Lorentz−Berthelot combining rules were applied. The Morse potential is given by

$$U_{Morse} = D_e(1 - e^{-\alpha(r-r_e)})^2 \tag{5}$$

where D_e, α, and r_e are the potential well depth, the empirical parameter, and the equilibrium minimum distance between the pair of atoms, respectively. The LJ and Morse parameters are taken from previous studies of thiol-SAM on the gold surface.[33,34] All interaction parameters used in this study are tabulated in Table 1.

II.2. Simulation Details. AuNPs with diameters of 4.0, 6.0, and 8.0 nm were built up using Material Studio 6.0,[35] which are essentially in a icosahedron shape with multiple facets with (111) and (100) planes. The nanoparticles, however, are approximately spherical. The structural aspect of ultrasmall gold nanoclusters, for example, organization and energy, has been well-discussed by Chaban and co-workers.[36−38] Different reactive force-fields are also developed to study the annealing of such nanoclusters.[39,40] However, in this work, we have used a fully flexible united atom model[41,42] to model the thiols, and atomistic AuNPs were considered. In the case of COOH-terminated alkyl thiols, the end group was modeled as atomistic for capturing the possible hydrogen bonding between such terminal groups. In this work, we have considered the following thiols for our study: *hexanethiol* (HT), *dodecanethiol* (DT), *6-mercaptohexanoic acid* (MHA), and *12-mercaptododecanoic acid* (MDA). In Figure 1, we have presented the initial structures of

Table 1. Force-Field Parameters

nonbonded parameters			
atoms	σ (Å)	ε (kcal/mol)	$q(e)$
Au	2.935	0.039	0
S	4.25	0.397	0
CH$_2$	3.905	0.118	0
CH$_3$	3.75	0.175	0
CH$_2$(CO)	3.905	0.118	0.12
C	3.9	0.08145	0.42
O(C)	3.05	0.157	−0.45
O(H)	3.02	0.185	−0.46
H	2.058	0.000	0.37

Morse potential			
pair	r_e (Å)	D_e (kcal/mol)	α
Au−S	2.65	8.763	1.47

bonded parameters		
bond	k_s (kcal/mol·Å^2)	r_0 (Å)
C−S	222.0	1.81
C−C	260.0	1.54
C−C(COOH)	260.0	1.52
C=O	980.0	1.214
C−O	750.0	1.364

angle	k_b (kcal/mol·rad^2)	θ_e (°)
S−C−C	116.7	114.7
C−C−C	120.6	109.47
C2−C=O	120.0	126.0
C2−C−O	140.0	111.0
C−O−H	160.0	107.0
O−C=O	160.0	123.0

dihedrals	k_1	k_2	k_3	k_4
C−C−C−C	0	0.666	−0.135	1.573
S−C−C−C	0	0.360	−0.106	1.530
C−C−O−H	0	2.748	0	0
O−C−O−H	0.750	2.748	0	0

Figure 1. Initial geometries for different systems simulated in this study: (a) single equilibrated drop of thiol placed in the vicinity of the nanoparticle, (b) nanoparticle dipped in a box filled with alkyl thiol, (c) two drops of different thiols placed away from each other with the nanoparticle in the center, (d) two drops placed in a Y arrangement with respect to the nanoparticle, and (e) two drops placed in a perpendicular manner with respect to the nanoparticle.

different systems used in this study. Figure 1a is the initial snapshot of the equilibrated droplet of thiol placed in the vicinity of the AuNP to understand the monolayer formation from the droplet. Spherical droplets of 1500 and 2000 thiol molecules of chain lengths C11 and C5, respectively, were prepared with different functional groups, namely, CH$_3$ and COOH. The thiol drops were equilibrated for 3.0 ns under NVT ensemble at 300 K, and then, these were placed in a close vicinity to the AuNP (Figure 1a). To find the correct/saturated number of thiols adsorbed on the AuNPs from the droplets, we set up a similar set of systems in which the AuNP was placed in the center of a thiol-filled box (Figure 1b). In the case of simulations with a thiol-filled box, under the NPT ensemble, we allowed the thiols to equilibrate for 2.0 ns without considering any special interaction (i.e., Morse potential) between gold and sulfur. After equilibration of thiols, we implemented a Morse potential between the pair. In the case of a double droplet, there may be three different scenarios (the details for considering three difference scenarios are given in the section under double droplet kinetics)—(a) the thiol droplets are placed away from each other with a nanoparticle in the center (Figure 1c); (b) the droplets are in a Y arrangement (Figure 1d), and (c) the droplets are in a perpendicular position with respect to the nanoparticle (Figure 1e). The gold atoms of the NPs were kept frozen during all simulations. In the case of the larger diameter AuNPs, the AuNPs were purposefully taken as

hollow spheres of skin thickness of 1.2 nm to enhance the computation efficiency. The adsorption behavior of thiols, however, was not found to be sensitive to the nature (solid or hollow) of the AuNPs. Simulations were carried out using the LAMMPS molecular dynamics software package.[43] The equations of motion were integrated with the Verlet algorithm[44] at a time step of 1.0 fs. The PPPM (particle−particle particle−mesh) technique[45] was used for the calculation of long-range electrostatic interactions. Periodic boundary conditions were used in all three Cartesian directions. All runs with the droplets were carried out in the canonical ensemble (NVT), maintaining the temperature at 300 K by applying the Nosé−Hoover thermostat[46,47] with a relaxation time of 0.1 ps. Systems with bulk thiols and nanoparticles were run under the isothermal−isobaric (NPT) ensemble, using the Nosé−Hoover thermostat[46,47] to maintain the temperature of the system constant (T = 300 K) and the Parrinello−Rahman barostat[48] to maintain its pressure constant (p = 1.0 bar and time constant = 1.0 ps). Simulations were carried out under the NPT ensemble for 20.0 ns for the bulk adsorption cases, 50−60 ns for single droplet cases, and 30 ns for mixed droplet cases. Additional 5−10 ns simulations were carried out to ensure the equilibration as the number of adsorbed molecules became static.

III. RESULTS AND DISCUSSION

We start the discussion with the monolayer formed on AuNPs when the nanoparticle is dipped into the bulk liquid thiols (Figure 1a). The growth dynamics of the monolayer on AuNPs of different diameters is studied by recording the time variation

of the number of thiols adsorbed on the AuNPs (N_{thiols}) and is shown in Figure 2. It is evident from Figure 2 that the
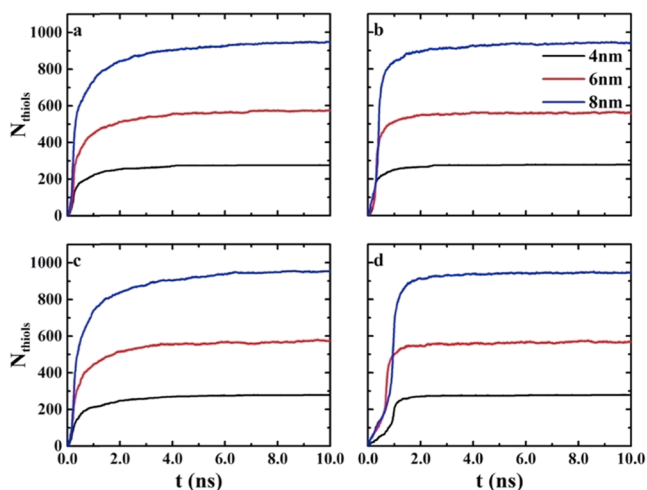
Figure 2. Time variation of the number of thiols, N_{thiols}, adsorbed on AuNPs of sizes 4.0, 6.0, and 8.0 nm from the bulk fluid thiols: (a) DT, (b) HT, (c) MDA, and (d) MHA.

Figure 3. Adsorption kinetics of thiols of different chain lengths and tail groups on AuNPs of sizes 4.0, 6.0, and 8.0 nm from the droplet of thiols: (a) HT, (b) DT, (c) MHA, and (d) MDA.

monolayer formation is a fast process because the monolayer gets saturated within 10.0 ns. The coating densities (number of thiols per nm^2) are found to be 8.29 ± 0.14, 5.11 ± 0.09, and 3.57 ± 0.03 for AuNPs of diameter 4.0, 6.0, and 8.0 nm, respectively, which are in line with the experimental findings (coating density of 8.62 and 8.02 thiols per nm^2 for 2.4 and 3.2 nm AuNPs, respectively) by Luedtke−Landman[49,50] and Hostetler et al.[51] [326 and 601 thiol molecules adsorbed on NPs with 2406 (~4 nm) and 6266 (~5.6 nm) Au atoms, respectively]. As the diameter increases, the radius of curvature decreases. The chain of thiol molecules require free volume to explore when they are bonded to the surface. The available free space for the chain of thiol molecules decreases with a decrease in the curvature, and hence, the number of thiols adsorbed per unit area decreases.

III.1. Single Droplet Kinetics. The formation of thiol coating on nanoparticles from a nanodroplet of alkyl thiols, with a diameter of 10.0 ± 0.5 nm, is kinetically different from that of dipping the nanoparticle into a pool of bulk thiols. Figure 3 presents the coating behavior of thiols with different terminal groups on AuNPs of different sizes. The thiol droplets considered in this work contain an excess number of thiols than that required for the formation of the monolayer. Thus, the process is not constrained because of the unavailability of thiols to form the monolayer. In the case of shorter alkyl thiols, for example, HT, the coating on AuNPs reached the saturation limit at ~10 ns on 4.0 nm AuNPs, as seen in Figure 3a. However, the growth of the monolayer is significantly slower compared with that of bulk fluid cases, where the saturation is reached within ~2 ns. The coating on 4.0 nm AuNPs reaches its saturation value of 290 thiols, which is similar to the value of the bulk case (see Figure 2). In the case of 6.0 nm AuNPs, the droplet takes more time compared with that of 4.0 nm because it reaches the saturation value of 620 only after ~16 ns, whereas the saturation value of the monolayer for 8.0 nm AuNPs is 1066 thiols, which is achieved at ~25 ns. It is interesting to note that the monolayers formed due to the nanodroplets of thiols contain more number of thiols, for a larger size of AuNPs, compared with those due to bulk thiols for which the
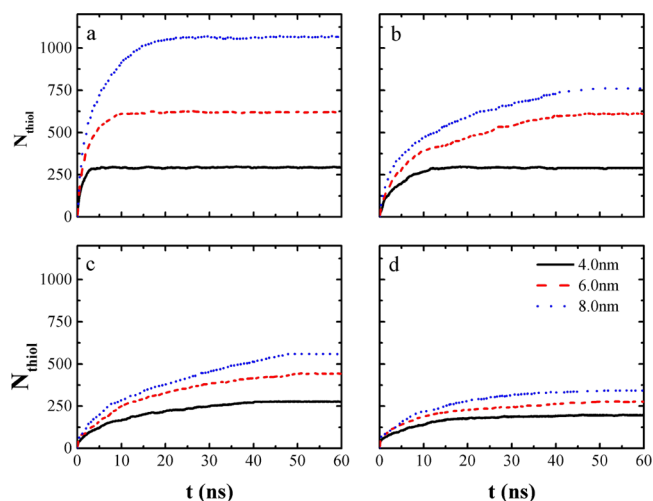
corresponding values for 4.0, 6.0, and 8.0 nm AuNPs are 278, 572, and 954, respectively. This is mainly attributed to the radial growth of the monolayer on AuNPs from the droplet of thiols, which allowed for a more compact arrangement of the molecules within that monolayer, as indicated by the higher number of adsorbed thiols. This is more visible with increasing size of the AuNPs. In the case of the DT drop (see Figure 3b), the monolayer growth is slower than that seen for HT. Adsorption of DT on 4.0 nm AuNPs reaches the saturation value of 290 thiol molecules within ~15 ns. On the other hand, it takes ~40 ns for 6.0 nm AuNPs to reach the plateau at 610. In the case of 8.0 nm, the adsorption reaches the plateau of 762 before reaching its saturation limit, in a time frame of ~45 ns. In the case of n-alkyl thiols, it takes a longer time to form a saturated monolayer from the DT droplet, whereas the HT monolayer is denser compared with that from the bulk thiol.

In the case of carboxylic-terminated thiols, that is, MDA and MHA, the adsorption process is even slower compared with that of n-alkyl thiols. The droplet of MHA, with a diameter of 10.0 ± 0.5 nm, is able to coat the 4.0 nm AuNPs, and the number of thiols adsorbed (277) is close to that of the alkyl thiols; whereas on larger AuNPs, the numbers are much less compared with the saturation value (see Figure 3c). For AuNPs of the other two sizes, 6.0 and 8.0 nm, the number of adsorbed thiols becomes constant at 443 and 560, respectively, beyond 45 ns (see Figure 3d), whereas the corresponding bulk values are 572 and 938. The plateau is reached after ~55 ns for 6.0 and 8.0 nm AuNPs. In the case of MDA (see Figure 3d), the number of thiols adsorbed is always less than that of bulk thiols. The plateau values are 196, 278, and 342 on 4.0, 6.0, and 8.0 nm AuNPs, respectively, obtained within the time frames of ~30, ~42, and ~45 ns. In the case of larger AuNPs, the number of thiol molecules adsorbed is much less than the saturation values, with two possibilities: either a partial coating with a similar packing density or distribution of molecules over the surface.

III.2. Kinetics Parameters. The kinetics of the formation of a monolayer from solutions of thiols onto the gold surface were well-studied by Jung and Campbell.[52,53] As pointed out by the authors, the simplest model to describe the time dependence of

adsorption of thiol molecules from solutions is a first-order Langmuir model

$$\theta = \theta_{\text{sat}}\left[1 - \sum_{i}^{2} x_i \exp(-t/\tau_i)\right] \tag{6}$$

where θ and θ_{sat} are the adsorbate coverage and its maximum or saturation coverage value, respectively, t is the time, τ_i is the time constant for adsorption, and x can be interpreted as the weighting parameter. Equation 6 is fitted in the data of adsorbate coverage with time, to obtain the time constants.

The resultant time scales, τ_1 and τ_2, governing the adsorption kinetics are tabulated in Table 2 (Figure S1). The first time

Table 2. Time Constants for Different Nanoparticles

d_{NP} (nm)	HT	DT	MHA	MDA
		τ_1 (ns)		
4.0	0.109	0.314	1.337	4.558
6.0	0.565	1.418	4.801	3.488
8.0	0.644	2.352	2.917	5.533
		τ_2 (ns)		
4.0	1.115	4.303	19.62	115.8
6.0	3.045	15.59	42.29	171.4
8.0	6.019	40.14	71.7	293.2

scale τ_1 corresponds to the bulk movement of the droplet, whereas the other time scale τ_2 can be attributed to the growth of the monolayers, which is the limiting step for the adsorption process. With increasing diameter of the nanoparticles, the time constants are found to increase for all thiols studied in this work. However, τ_1 is usually small in value (<6 ns) for all cases. In the case of adsorption from bulk thiols, the kinetics is better fitted with the first-order Langmuir model and is better interpreted as a single-step adsorption, with the time constant being in the range of 0.3–0.8 ns.

In the case of HT, the lower values of the time constants are clearly an indication of a fast adsorption process. Nevertheless, the growth process becomes slower for larger AuNPs. In addition, as the chain length increases, the time constant also increases, as inferred by the inspection of the τ_2 values of DT, which are 1 order of magnitude higher than that of HT. The time constants of MHA and DT are of the same order, whereas MDA has time constants with its magnitude 1 order higher than the former thiols.

The next step is to clarify the role played by diffusion in the growth dynamics of the monolayer. The self-diffusion coefficient D calculated for all thiols in bulk is shown in Table 3. The COOH-terminated thiols have lower diffusion coefficients compared with those of DT and HT; in fact, a difference of 2 orders of magnitude is observed in D values between methyl- and carboxyl-terminated thiols. Here, by trying to correlate the self-diffusion coefficient with the time constants, nonlinear relationships, $\tau_i = A_i \times D^{mi}$ (A and m being

Table 3. Self-Diffusion Coefficients of Different Thiols in an Unadsorbed State

thiol type	D_{self} (cm^2/s)
HT	$3.16 \pm 0.02 \times 10^{-7}$
DT	$1.11 \pm 0.01 \times 10^{-7}$
MHA	$1.06 \pm 0.02 \times 10^{-8}$
MDA	$3.47 \pm 0.02 \times 10^{-9}$

constants), are attained for different diameters of nanoparticles. Such relationships are presented in Figure S2, along with the m values that are calculated from the logarithmic plots. From the m values for τ_1 and τ_2, it can be seen that τ_1 shows a weaker dependency on D (the average value of m_1 is −0.535, calculated from the slope of the fitted lines in Figure S2b) than τ_2 (for which the average value of m_1 is −0.825). Thus, it appears that the diffusion process dominates beyond the regime of τ_1. Further, for both the time constants, the m values increase as the diameter of AuNPs increases. However, a linear dependency is observed between the radius of curvature of the nanoparticles and m (see Figure S2). τ_1 has a higher dependency (a higher negative slope, −1.640) on the radius of curvature compared with τ_2. Overall, the time constants are correlated with the diffusion coefficients of thiols and the diameter of nanoparticles by a relation of the type, $\tau = AD^{C+B/d\text{NP}}$, where B and C are constants (see eqs S1 and S2).

III.3. Monolayer Distribution from a Single Droplet. To show the distributions of the monolayer formed on AuNPs, we have calculated the density of the sulfur atom of thiols in the spherical polar coordinate system with θ and ϕ as azimuthal and polar angles, respectively. The density contour plots, given in Figure 4, show such distributions related to HT (a−c) and DT (d−f) on different AuNPs. As can be seen, a uniform distribution of HT is observed, thus indicating a continuous monolayer for all different sizes of AuNPs. Further, the corresponding snapshots of the coated nanoparticles, given at the right-hand side of Figure 4a−c, also clearly indicate a uniform coating on the AuNP surface. Figure 4d−f shows the distributions of DT on different AuNPs and the corresponding equilibrated snapshots of the coated AuNPs. For the smaller diameters of AuNPs viz., 4.0 and 6.0 nm (Figure 4d,e, respectively), the observed uniform distribution for DT is similar to that of the distribution seen for HT (see Figure 4a−c). It shows a uniformly distributed monolayer on the AuNP surface for smaller diameters (Figure 4d). However, for the case of 8.0 nm AuNPs, the vacant area at the center of the contour diagram (Figure 4f) indicates an incomplete coating. The incomplete coating can also be noticed from the snapshot of the coated AuNPs of 8.0 nm size at 50 ns.

We have already seen that for COOH-terminated thiols, the kinetics is much slower compared with that for alkyl thiols. Figure 5 shows the distribution of COOH-terminated thiols on different AuNP sizes. In the case of the MHA droplet (Figure 5a−c) on 4.0 nm AuNPs, the monolayer contains a number of thiols closer to its saturation value, and thus, it is expected to form a uniform coating that is also clear from the contour diagram shown in Figure 5a. The snapshot presented in Figure 5a (right to the contour plot) also justifies such a uniform coating. In the case of 6.0 and 8.0 nm AuNPs, the number of thiols adsorbed on the surface is less than the saturation value. Hence, in the density contour diagram of these two cases, a partial coating is observed, which is also reflected in the snapshots shown in Figure 5b,c. In the case of MDA droplets (Figure 5d−f), the value of the number of thiols adsorbed on the AuNPs is even more far away from its saturation value compared with that of MHA coating. That deviation increases as the diameter of the AuNPs increases, leading to an increased amount of incomplete coating, which in turn also increases with increasing AuNP diameter. One can observe the above trend through the increased vacant region in the corresponding contour diagram and the island portion in the snapshots as the diameter of the AuNPs increases (see Figure 5d−f).
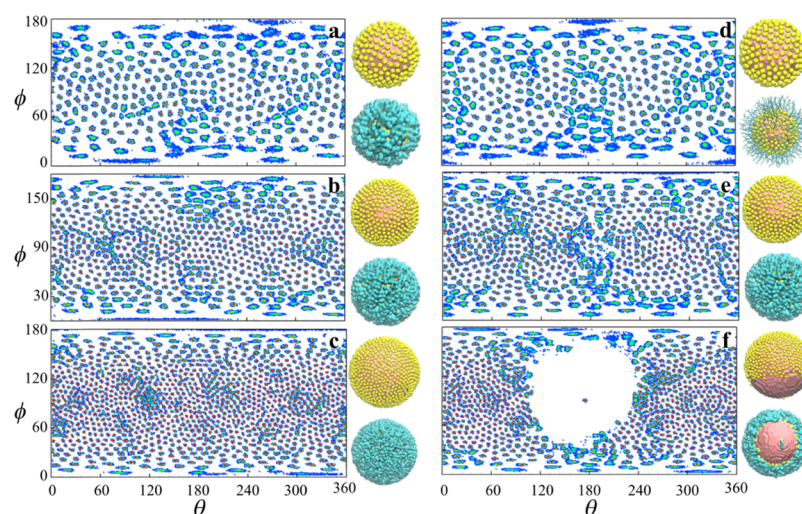
Figure 4. Number density distribution of HT (a−c) and DT (d−f) adsorbed on AuNPs of different sizes and the corresponding snapshots of the AuNPs with coated sulfur atoms (yellow) and coated SAMs (cyan color). The sizes of AuNPs are 4.0 nm (top layer), 6.0 nm (middle layer) and 8.0 nm (bottom layer). White color represents vacant space and the color transition blue-green-red pertains to an increasing value of the number density.
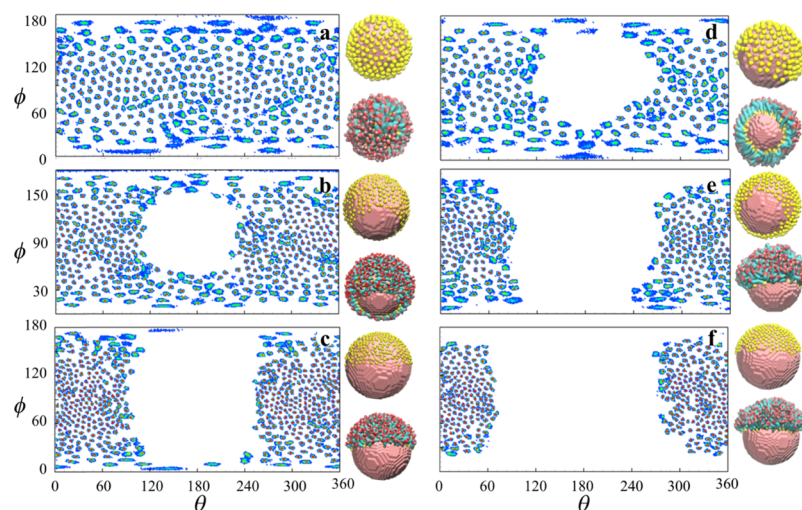
Figure 5. Number density distribution of MHA (a−c) and MDA (d−f) adsorbed on AuNPs of different sizes and the corresponding snapshots of the AuNPs with coated sulfur atoms (yellow) and coated SAMs (cyan color). Color and size descriptions are the same as in Figure 4. Here, oxygen atoms are colored in red.

III.4. Propagation Mechanism. We have analyzed the dynamics of the monolayer formation on AuNPs, and typical snapshots of the partially covered AuNPs for two different thiols are shown in Figure 6. First, we will discuss the cases of alkyl thiols. At the very beginning, the droplets will adhere to the surface and the available S-atoms will bind to the Au surface. After the formation of the initial coating, the surface of the nanoparticle is shielded by the monolayer that essentially creates a barrier for the unadsorbed thiols. To further propagate the monolayer, a molecule needs to diffuse over the existing monolayer. In the case of HT, the diffusion over the monolayer is expected to be easier because of the lower interchain interaction between HT molecules (−14.07 kcal/mol) compared with DT (−24.67 kcal/mol for undecane-1-thiol). The adsorption energies of the two alkyl thiols are −57.42 and −60.65 kcal/mol.[54] Thus, for alkyl thiols, the propagation of the monolayer is restricted even when there is a large excess of thiols present. Nevertheless, the mechanism of propagation is different for COOH-terminated thiols. Because of the presence
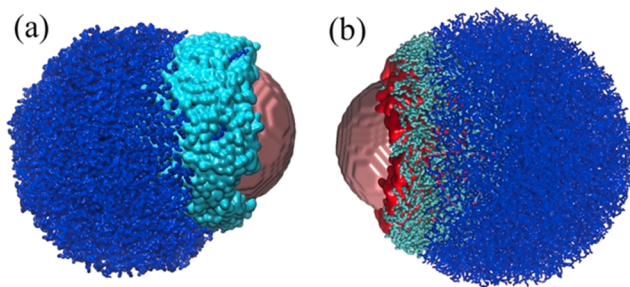
Figure 6. Monolayer propagation for (a) CH₃-terminated thiols and (b) COOH-terminated thiols. Color coding and representations are the following: pink sphere—AuNPs, blue sticks—thiols that are not in the monolayer, cyan surface—monolayer of alkyl thiols, red surface—monolayer of mercaptocarboxylic acids, and light blue sticks—molecules that are bonded with the monolayer of COOH-terminated thiols.

of the COOH group, the intermolecular hydrogen bonding leads to a lowering of the bulk diffusion of thiols (interchain interaction energies are −22.37 and −33.67 kcal/mol for MHA and 11-mercaptoundecanoic acid, respectively).[54] The already formed monolayer remains hydrogen bonded with the nearest molecules that are under strong attractive forces coming from the remaining thiols. Thus, a network of hydrogen bonds is essentially created with the adsorbed monolayer and the drop. The higher surface tension of these thiols hinders the molecule to escape from the drop by retaining its size. Thus, the propagation of the monolayer involves coverage of the nanoparticle by the whole droplet. With increased drop size, the network becomes more flexible and slower propagation continues, and it will be discussed in the next section.

III.5. Effect of Droplet Size. To understand the effect of the size of the droplet on the kinetics and the formation of a monolayer on the AuNPs, we have simulated the adsorption of thiols using different sizes of droplets on 8.0 nm AuNPs. We took droplets with 3000 and 5000 molecules of C11 chain and 4000 and 6000 molecules of C5 chain. The time variation in the number of adsorbed thiols for C5 and C11 is shown in Figure S3. In Figure S3, for CH₃-terminated thiols (solid lines), superimposing adsorption isotherms are observed for different droplet sizes, indicating that the surfaces occupied by the thiols appear to behave similarly for different droplet sizes (see Table 4). The variation in the number of CH₃-terminated thiols

Table 4. Number of Thiols Adsorbed on 8 nm NP from the Variable Volume of the Droplet

| thiol | number of thiols adsorbed | | | |
	droplets with 2000 thiols	droplet with 4000 thiols	droplet with 6000 thiols	bulk
HT	1066 ± 5	1089 ± 9	1093 ± 6	954 ± 12
MHA	560 ± 3	801 ± 4	842 ± 3	942 ± 7
thiol	droplet with 1500 thiols	droplet with 3000 thiols	droplets with 5000 thiols	bulk
DT	762 ± 3	730 ± 6	725 ± 4	948 ± 5
MDA	334 ± 6	553 ± 7	710 ± 3	941 ± 4

adsorbed is negligible compared with that of the other kind. As compared with the value, HT droplets constitute a closely packed monolayer and DT molecules also form a packed monolayer; however, the surface remains unsaturated. On the other hand, for COOH-terminated thiols (dashed lines), the coverage increases with increasing size of the droplets, as evident from Figure S3. As the monolayer grows from the side of the thiol droplet, the monolayer density is found to be the same as that obtained from single droplets (Figure 2). The time constants, obtained by fitting the kinetic data to eq 6, are plotted against the diameter of the droplets, as shown in Figure S4. The τ_1 values for different droplet sizes of HT and DT are almost the same order of magnitude. However, a slight decrease in τ_1 is observed for MDA and MHA with increasing size of the droplets. In the case of the characteristic time scale τ_2 of the diffusion control step, a higher degree of dependency on the droplet sizes can be observed for the COOH-terminated thiols. In the case of HT and DT, the value almost remains constant. In the case of MHA, the value decreases with increasing size by 55 and 65%. Further, a decrease in the time constant is observed for MDA, where the reductions are 73 and 87% for higher droplet sizes.

So far, we have discussed the kinetics of the formation of a monolayer from a single droplet of thiol on nanoparticles of different diameters. The kinetic data clearly show different time scales for the two-step propagation, which involves fast adsorption followed by a diffusion-governed adsorption. But as noticed, the latter one has different mechanisms for different terminal groups. The difference in the kinetic behavior of monolayers seen for different thiols can be used to create a Janus coating from double droplets system, as discussed in the next section.

III.6. Double Droplet Kinetics. Janus coating requires two unique functionalities on the AuNP surface. In this work, hydrophilicity and hydrophobicity are imparted to provide Janus nature for the AuNPs. To do so, we considered two droplets of alkyl thiol and mercapto-carboxylic acid placed far away from each other to avoid mixing before forming the monolayer. Four combinations are used in this work, namely, (1) DT-MDA; (2) HT-MDA; (3) DT-MHA; and (4) HT-MHA. Using the self-assembly method, computational[22] and experimental studies[23] have showed that the size of the nanoparticle can alter the self-assembly of the coated layer. For example, stripe formation was observed for 4.5 nm AuNPs, but it becomes Janus as the diameter is reduced to 1.5 nm. To investigate the effect of radius of curvature on the formation of Janus coating, here, we considered 4, 6, and 8 nm size AuNPs. Janus coating may be affected by changing the position of thiol droplets. There are two different initial configurations, namely, Y-shape and T-shape (see Figure 7a,b) that are being used in
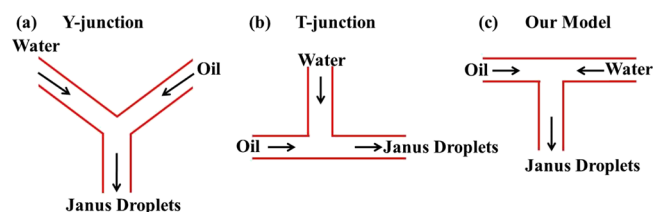
Figure 7. Schematic presentation of different arrangements and our model.

the Pickering emulsion technique for the synthesis of JPs. Our results from the single droplet adsorption gives an indication that Y- and T-shape geometries may lead to a more contaminated JP or a higher JB (> 0.8). Also, it may provide an unsaturated coating for larger size AuNPs. Hence, to overcome the above issues, we proposed the modified T-model, which is shown in Figure 7c. For our convenience, experimental T-shape geometry and our proposed T-shape geometry are hereafter called as ET and OT, respectively. To prove our assumption on the formation of Janus coating using Y- and ET-shape geometries, we have conducted simulations for the case of composition 1, that is DT-MDA with Y (all three sizes of AuNPs) and ET (8 nm AuNPs) arrangements. Figure 1c−e shows the initial structures of the systems when the two droplets are in opposite sides (OT), at the same side (Y), and at 90° to each other (ET). The adsorption kinetics of different pairs for the cases where the droplets are in opposite sides (OT-shape geometry) is shown in Figure 8. As can be seen, the overall kinetics of formation of the monolayer is much faster compared with the cases of single droplets. Comparison of the time constants clearly depicts faster kinetics for the several kinds of double droplets. Because of the different compositions on three different sizes of AuNPs, we observed different coating
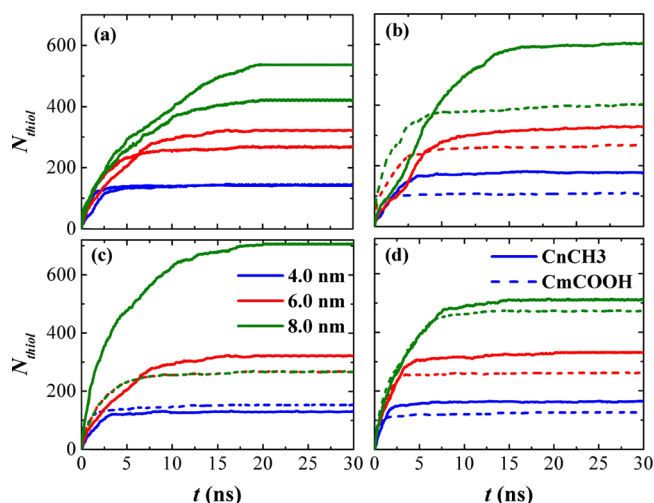
Figure 8. Adsorption kinetics of thiols from two droplets of different combinations of chain lengths and tail groups on AUNPs of sizes 4.0 nm (blue), 6.0 nm (red), and 8.0 nm (green). Four different combinations are presented, namely, DT-MDA (a), HT-MDA (b), DT-MHA (c), and HT-MHA (d). Solid and dashed lines are representative of the different terminal groups CH_3 and COOH, respectively.

times and N_{thiol} values for a particular type of thiol when it is mixed with other types. In the case of DT-MDA pair, the adsorption isotherms of two thiols are identical for smaller 4.0 nm AuNPs (Figure 8a). The composition of the monolayer becomes stable after ~10.0 ns. In the case of 6.0 nm AuNPs, MDA is adsorbed at a faster rate (~7 ns) compared with that of DT (~15 ns). At the beginning (less than 7 ns), the number of adsorbed MDA is greater than that of DT, but subsequently, it is reversed, that is, the number of adsorbed DT is greater than that of MDA. Similarly, for 8.0 nm AuNPs, less number of MDA adsorbs compared with that of DT. Notice here that the number of adsorbed MDA is approximately the same for all three sizes of AuNPs, with the same composition of the droplets in the Y arrangement, as shown in Figure S5. Thus, in the case of Y arrangements, the number of adsorbed DT will be

higher in comparison with that of the OT arrangement, and it is found to be true for 4.0 nm AuNPs. However, in the case of 6.0 and 8.0 nm AuNPs, the closer proximity of the larger size droplets allowed them to mix with each other and the DT molecules spread over the MDA droplet that caused retardation of the growth of the DT monolayer (see Figure S6). This essentially becomes equivalent to the propagation of the monolayer from a single droplet, as one can infer from Movie S1 and Figure S7. For comparison, we have plotted the total N_{thiol} for Y-shape geometry versus single droplet cases in Figure S7. As we can see from Figure S4, the total N_{thiol} (DT + MDA) adsorbed from the double droplet is similar to that of a single droplet. The deviation, however, is due to the presence of MDA, which shows a faster initial adsorption followed by a slower diffusion-controlled adsorption. Also, the layering of DT on the MDA droplet essentially retards the growth of the MDA monolayer and slows its own growth on the nanoparticle. Movie S2 shows the Janus monolayer formation on 8.0 nm AuNPs from ET-shape geometry. The adsorption behavior is similar to that of Y-shape geometry, namely, unsaturated coating, retardation of the MDA monolayer growth, and layering of DT on the MDA droplet. In the case of composition (2), the number of adsorbed molecules is higher for HT for all sizes of nanoparticles (see Figure 8b). Though in all cases, initially, adsorption of MDA is higher compared with that of HT, MDA reaches the plateau in a quick time (~2−5 ns). On the other hand, the HT molecules still spread over the wetted surface to occupy the rest of the surface. As the diameter of the AuNPs increases, the difference between the number of adsorbed molecules increases, which is evident from Figure 8b. In the case of composition (3), a monolayer on 4.0 nm AuNPs becomes stable within ~10 ns (see Figure 8c). The number of DT is less compared with that of MHA. In the case of larger AuNPs, the MHA adsorption shows a similar adsorption with time, whereas the DT values reach the plateau at about 15 and 19 ns, for 6.0 and 8.0 nm AuNPs, respectively. We have found that the difference between the number of thiols adsorbed for composition (4) (see Figure 8d) is small ($\Delta N_{thiol} \approx$ 30−60), with a higher value for HT. It is evident that the HT molecules, because of higher diffusion, are able to
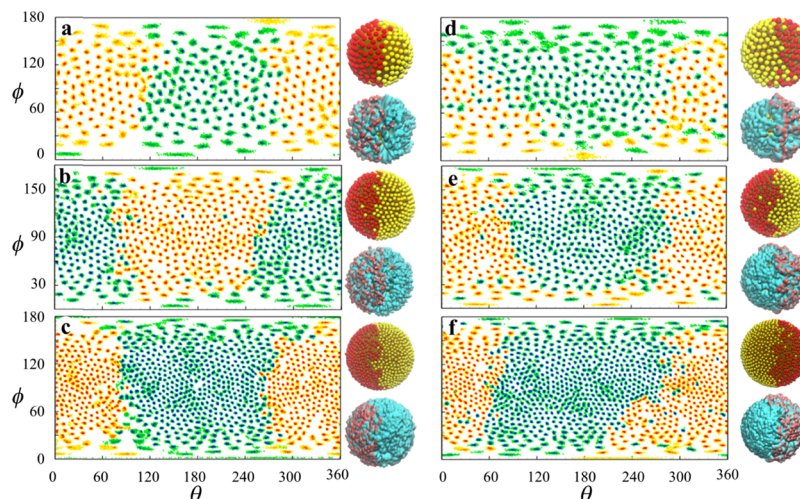
Figure 9. Number density distributions of DT (green-blue contour)-MDA (yellow-red contour) (a−c) and HT (green-blue)-MDA (yellow-red) (d−f) adsorbed on the surfaces of AuNPs of different sizes, 4.0 (a,d), 6.0 (b,e), and 8.0 nm (c,f). Snapshots of the SAM (cyan for alkyl thiol and red for COOH-terminated thiol) and sulfur atoms (yellow and red spheres for alkyl thiols and COOH-terminated thiols, respectively) adsorbed on the nanoparticle are shown in the right side of each contour diagram. White color represents the vacant space.
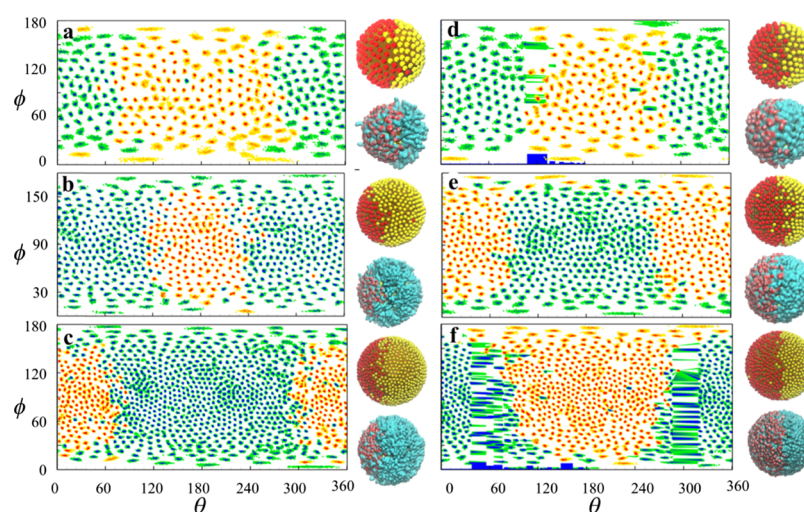
Figure 10. Number density distributions of DT (green-blue contour)-MHA (yellow-red contour) (a−c) and HT (green-blue)-MHA (yellow-red) (d−f) adsorbed on the surfaces of AuNPs of different sizes, 4.0 nm (a,d), 6.0 nm (b,e), and 8.0 nm (c,f). The color scheme is the same as in Figure 9.

occupy more surfaces compared with that of MDA. Though we have started the adsorption of thiols from two different droplets, which are sufficiently far away from each other, one need to check the distribution of thiols on Janus coating. This distribution will provide qualitative information about the mixing nature (completely mixed/demixed) of the thiols and the surface coverage, and hence we present the same analysis in the following section.

III.7. Monolayer from Double Droplets. To sketch the uniformity of the monolayer, density contour diagrams of thiols adsorbed on the AuNPs are plotted, using the same procedure discussed earlier for single droplets. For DT-MDA droplets, the monolayer compositions are shown in Figure 9a−c. In the case of 4.0 nm AuNPs (Figure 9a), two very clear faces are formed. At the interface, some mixing is observed that occurs at the later stages. Initially, the MDA drop coats as much as possible, though the density remains lower in the wetted face. Near saturation, rearrangement of the molecules allows more accommodation, causing these contaminations. The snapshot of the coated AuNPs shown in Figure 9a also depicts the faces formed. However, the mixing near the interface is not clearly visible. Similarly, in the case of 6.0 nm AuNPs, the mixing is of a similar extent as seen in the 4.0 nm AuNPs. The contour diagram (cf. Figure 9b) shows that the mixing of few DT occurred into the MDA region, which can be observed in the snapshots at the right-hand side also. In the case of 8.0 nm NPs, the contaminations are even less, and a nicely packed monolayer with a distinct separation line can be observed (see Figure 9c). However, in the case of Y-shape geometry, the number of MDA adsorbed in the monolayer is lower (73−93) compared with that of OT-shape. DT molecules spread over the surface of the nanoparticle after fusing with the MDA droplet. The propagation of the monolayer is found to be the same as that observed in the case of single droplets of alkyl thiols.

Similarly, in the case of HT-MDA, more contaminations are observed on the monolayer for different sizes of AuNPs (see Figure 9d−f). Initially, adsorption of MDA is higher (as seen in Figure 8b) and leads to the formation of a monolayer with a sparse packing. The smaller size of HT molecules makes it more susceptible to penetrate on the already formed MDA layer on the surface because MDA molecules rearrange

themselves. Similarly, for the other two 6.0 and 8.0 nm NPs (Figure 9b,c, respectively), a higher degree of contamination may be observed compared with that of DT-MDA. In the contour diagrams, blue-green dots appear in the yellow-red region, but no yellow-red dots are seen in the blue-green region. These observations clearly indicate that HT molecules diffuse into the monolayer formed by MDA, but the vice versa is not observed. The right side of the contour plots in Figure 9 shows the snapshots of the monolayer. In these images, finding the mismatches is difficult because longer MDA molecules occupy the space over the smaller HT molecules. In the case of the DT-MHA pair depicted in Figure 10, dependency of the monolayer composition on the AuNP diameter can be observed. In the case of 4.0 nm AuNPs, the number of adsorbed DT is less than that of MHA (cf. Figure 8c). In the contour diagram (cf. Figure 10a−c), appearance of blue-green dots indicate contamination in the MHA monolayer on nanoparticles of different diameters. However, there are no significant contaminations of MHA in the DT faces. The coating formed by the HT-MHA pair (see Figure 10d−f) reveals very less contamination. Smaller chains of HT are shown to diffuse more into the droplet of MHA, and some HT is found in the MHA faces. However, the mixing is not very extensive for different diameters of the AuNPs (cf. Figure 10d−f). The snapshots of the coated AuNPs displayed in the right side of the contour plots in Figure 10d−f provide evidence for highly separated faces. In the case of Y-shape arrangement of the droplets and the nanoparticle, the nature of the coating remains the same with a small coating of carboxyl thiols (see Figures S5, S6 and Movies S1, S2). In these cases, after the initial growth of the monolayer by both droplets, the droplets collapse on one another. The CH$_3$-terminated thiols form a layer around the droplet of COOH-terminated thiols and hinder the growth of the monolayer of COOH-terminated thiols. The growth of the monolayer is dominated by alkyl thiols, and the growth mechanism is similar to that of single droplets. Our results show that the double droplets in the OT arrangement yield saturated adsorption for all cases, particularly even for the case of larger AuNPs consisting of a longer thiol with COOH terminal groups.

Although the results from growth kinetics and density contour for mixed droplets show the surface asymmetry on JPs,

the ratio between the two functionalities (JB) gives more quantitative value for the surface asymmetry. Hence, in the next section, we will discuss the JB for all cases.

III.8. JB. From the contour diagrams for different droplet mixtures, we calculated the JB (β), which is defined as the ratio of the area covered by alkyl thiols to the surface area of AuNPs. The JBs obtained from different combinations are listed in Table 5. As a result of the observed faster coating and diffusion

Table 5. JB (β) at Different Droplet Combinations and Size of AuNPs (d_{NP})

d_{NP} (nm)	droplet combinations			
	DT-MDA	DT-MHA	HT-MDA	HT-MHA
4.0	0.495	0.458	0.620	0.558
6.0	0.547	0.547	0.550	0.557
8.0	0.560	0.715	0.600	0.520

for alkyl thiol than that of COOH-terminated thiol from the study of single thiol droplets, here, we have observed larger alkyl thiol segregation in the JPs for all cases except for the case of DT-MDA and DT-MHA on 4.0 nm AuNPs. The amount of alkyl thiol segregation in JPs varies with respect to the length of the COOH-terminated thiol and the size of AuNPs. In the case of 4.0 nm AuNPs coated with DT-MDA and with DT-MHA, β is less than 0.5. In the case of COOH-terminated thiols, the sulfur atoms remain in the periphery of the droplet because COOH groups form intermolecular hydrogen bonding in the core. Higher availability of sulfur atoms at the periphery allows faster propagation of the monolayer initially, after which the diffusion of COOH thiols starts, retarding the propagation. In both cases, the alkyl thiol that has a longer chain is DT. In contrast to the COOH thiol droplet, the longer chains hide the sulfur atoms in the core in the DT droplet, which leads to a slower initial diffusion. Because the size of the AuNPs is smaller, the time difference is just enough for the COOH-terminated thiols to occupy more area compared with that of DT. In larger AuNPs, the higher diffusion of alkyl thiols overcomes the initial advantages of occupying the majority of the monolayer and provides higher values of β. It is worth noting that, in this work, we could get JPs for all sizes of AuNPs studied in this work. Hence, our results of formation of Janus coating on three different sized AuNPs with different thiols help us conclude that this method shows size independency of AuNPs for Janus coating. Further, our results show that the desired JB can be achieved by altering the chain length of the thiol with the terminal groups and the size of the AuNPs.

IV. CONCLUSIONS

In this work, we have used molecular dynamics to study the propagation of monolayer of thiols with different terminal groups on AuNPs of different sizes under extremely bad solvent conditions. A two-step growth of the thiol monolayer on the nanoparticle is found: first, spreading of thiols because of binding of the droplet, which is followed by the diffusion-dominated growth. The initial step is found to be fast (~1 ns), whereas the latter one is much slower (~100 ns). Moreover, the kinetics of the growth of the thiol monolayer is dependent on the size of the nanoparticles, on the self-diffusion coefficient of thiols, and on the diffusion of thiols over the nascent monolayer. In the case of COOH-terminated thiols, its strong hydrogen-bonding network hinders the propagation process and thus has slower kinetics of adsorption. We have also seen

that the effect of the droplet size is negligible for alkyl thiols, whereas the area covered by the monolayer increases with the increase in the drop size for COOH-terminated thiols. Further, we have studied the formation of Janus coating from droplets of thiols by using the kinetics of different thiols. The segregation degree of the two thiols on JPs was estimated through JB. In our study, we have obtained Janus coating on the AuNPs with a variable JB in the range of 0.45−0.72 for different diameters of the AuNPs. For instance, in the case of shorter chain length mixing, the JB of JPs is independent of the AuNP size, and the other case of equal longer thiol mixing and unequal mixing shows various values of JB on JPs. Hence, our results lead us to conclude that one can achieve the desired JPs by choosing the appropriate chain length of the thiol and the size of AuNPs.

■ ASSOCIATED CONTENT

Ⓢ Supporting Information

The Supporting Information is available free of charge on the ACS Publications website at DOI: 10.1021/acs.langmuir.6b04680.

> Variation of the time constants with the diameter of the nanoparticles, logarithmic plot of the time constants and self-diffusion coefficient correlations, time variation of the number of adsorbed thiols on 8.0 nm size AuNPs, variation of the time constants with the diameter of the droplets, adsorption kinetics of thiols in the case of Y arrangement of two droplets of DT-MDA on AuNPs of sizes 4, 6, and 8 nm, and number density distribution of DT and MDA adsorbed on the surfaces of AuNPs of sizes, 4, 6, and 8.0 nm (PDF)
>
> Propagation of monolayer on 8.0 nm AuNPs when the droplets are in Y-geometry. Movie S1 (MPG)
>
> Propagation of monolayer on 8.0 nm AuNP when the droplets are in ET arrangement. Movie S2 (MPG)

■ AUTHOR INFORMATION

Corresponding Author
*E-mail: jayantks@iitk.ac.in.
ORCID Ⓞ
Debdip Bhandary: 0000-0001-7118-1724
Notes
The authors declare no competing financial interest.

■ REFERENCES

(1) Walther, A.; Müller, A. H. E Janus particles: Synthesis, self-assembly, physical properties, and applications. *Chem. Rev.* **2013**, *113*, 5194−5261.

(2) Lattuada, M.; Hatton, T. A. Synthesis, properties and applications of Janus nanoparticles. *Nano Today* **2011**, *6*, 286−308.

(3) Xu, K.; Guo, R.; Dong, B.; Yan, L.-T. Directed self-assembly of Janus nanorods in binary polymer mixture: Towards precise control of nanorod orientation relative to interface. *Soft Matter* **2012**, *8*, 9581−9588.

(4) Yan, L.-T.; Popp, N.; Ghosh, S.-K.; Böker, A. Self-assembly of Janus nanoparticles in diblock copolymers. *ACS Nano* **2010**, *4*, 913−920.

(5) Christian, D. A.; Tian, A.; Ellenbroek, W. G.; Levental, I.; Rajagopal, K.; Janmey, P. A.; Liu, A. J.; Baumgart, T.; Discher, D. E. Spotted vesicles, striped micelles and Janus assemblies induced by ligand binding. *Nat. Mater.* **2009**, *8*, 843−849.

(6) Semrau, S.; Schmidt, T. Membrane heterogeneity—from lipid domains to curvature effects. *Soft Matter* **2009**, *5*, 3174−3186.

(7) Semrau, S.; Idema, T.; Holtzer, L.; Schmidt, T.; Storm, C. Accurate determination of elastic parameters for multicomponent membranes. *Phys. Rev. Lett.* **2008**, *100*, 088101.

(8) Gangwal, S.; Cayre, O. J.; Velev, O. D. Dielectrophoretic Assembly of Metallodielectric Janus Particles in AC Electric Fields. *Langmuir* **2008**, *24*, 13312−13320.

(9) Kim, S.-H.; Jeon, S.-J.; Jeong, W. C.; Park, H. S.; Yang, S. M. Optofluidic Synthesis of Electroresponsive Photonic Janus Balls with Isotropic Structural Colors. *Adv. Mater.* **2008**, *20*, 4129−4134.

(10) Valadares, L. F.; Tao, Y.-G.; Zacharia, N. S.; Kitaev, V.; Galembeck, F.; Kapral, R.; Ozin, G. A. Catalytic nanomotors: Self-propelled sphere dimers. *Small* **2010**, *6*, 565−572.

(11) Gibbs, J. G.; Zhao, Y.-P. Autonomously motile catalytic nanomotors by bubble propulsion. *Appl. Phys. Lett.* **2009**, *94*, 163104.

(12) Suci, P. A.; Kang, S.; Young, M.; Douglas, T. A streptavidin−protein cage Janus particle for polarized targeting and modular functionalization. *J. Am. Chem. Soc.* **2009**, *131*, 9164−9165.

(13) Kang, S.; Suci, P. A.; Broomell, C. C.; Iwahori, K.; Kobayashi, M.; Yamashita, I.; Young, M.; Douglas, T. Janus-like protein cages. Spatially controlled dual-functional surface modifications of protein cages. *Nano Lett.* **2009**, *9*, 2360−2366.

(14) Hu, S.-H.; Gao, X. Nanocomposites with spatially separated functionalities for combined imaging and magnetolytic therapy. *J. Am. Chem. Soc.* **2010**, *132*, 7234−7237.

(15) Daniel, M.-C.; Astruc, D. Gold nanoparticles: Assembly, supramolecular chemistry, quantum-size-related properties, and applications toward biology, catalysis, and nanotechnology. *Chem. Rev.* **2004**, *104*, 293−346.

(16) Thomas, K. G.; Kamat, P. V. Chromophore-functionalized gold nanoparticles. *Acc. Chem. Res.* **2000**, *36*, 888−898.

(17) Shipway, A. N.; Katz, E.; Willner, I. Nanoparticle arrays on surfaces for electronic, optical, and sensor applications. *ChemPhysChem* **2000**, *1*, 18−52.

(18) Takei, H.; Shimizu, N. Gradient sensitive microscopic probes prepared by gold evaporation and chemisorption on latex spheres. *Langmuir* **1997**, *13*, 1865−1868.

(19) Velev, O. D.; Lenhoff, A. M.; Kaler, E. W. A class of microstructured particles through colloidal crystallization. *Science* **2000**, *287*, 2240−2243.

(20) Cayre, O.; Paunov, V. N.; Velev, O. D. Fabrication of asymmetrically coated colloid particles by microcontact printing techniques. *J. Mater. Chem.* **2003**, *13*, 2445−2450.

(21) Roh, K.-H.; Martin, D. C.; Lahann, J. Biphasic Janus particles with nanoscale anisotropy. *Nat. Mater.* **2005**, *4*, 759−763.

(22) Singh, C.; Ghorai, P. K.; Horsch, M. A.; Jackson, A. M.; Larson, R. G.; Stellacci, F.; Glotzer, S. C. Entropy-mediated patterning of surfactant-coated nanoparticles and surfaces. *Phys. Rev. Lett.* **2007**, *99*, 226106.

(23) Kim, H.; Carney, R. P.; Reguera, J.; Ong, Q. K.; Liu, X.; Stellacci, F. Synthesis and Characterization of Janus Gold Nano-particles. *Adv. Mater.* **2012**, *24*, 3857−3863.

(24) Nisisako, T.; Torii, T.; Takahashi, T.; Takizawa, Y. Synthesis of monodisperse bicolored janus particles with electrical anisotropy using a microfluidic co-flow system. *Adv. Mater.* **2006**, *18*, 1152−1156.

(25) Nisisako, T.; Torii, T. Formation of Biphasic Janus Droplets in a Microfabricated Channel for the Synthesis of Shape-Controlled Polymer Microparticles. *Adv. Mater.* **2007**, *19*, 1489−1493.

(26) Chen, C.-H.; Shah, R. K.; Abate, A. R.; Weitz, D. A. Janus particles templated from double emulsion droplets generated using microfluidics. *Langmuir* **2009**, *25*, 4320−4323.

(27) Shah, R. K.; Kim, J.-W.; Weitz, D. A. Janus Supraparticles by Induced Phase Separation of Nanoparticles in Droplets. *Adv. Mater.* **2009**, *21*, 1949−1953.

(28) Andala, D. M.; Shin, S. H. R.; Lee, H.-Y.; Bishop, K. J. M. Templated Synthesis of Amphiphilic Nanoparticles at the Liquid−Liquid Interface. *ACS Nano* **2012**, *6*, 1044−1050.

(29) Liu, X.; Yu, M.; Kim, H.; Mameli, M.; Stellacci, F. Determination of monolayer-protected gold nanoparticle ligand−shell morphology using NMR. *Nat. Commun.* **2012**, *3*, 1182.

(30) Iida, R.; Kawamura, H.; Niikura, K.; Kimura, T.; Sekiguchi, S.; Joti, Y.; Bessho, Y.; Mitomo, H.; Nishino, Y.; Ijiro, K. Synthesis of Janus-like gold nanoparticles with hydrophilic/hydrophobic faces by surface ligand exchange and their self-assemblies in water. *Langmuir* **2015**, *31*, 4054−4062.

(31) Glogowski, E.; He, J.; Russell, T. P.; Emrick, T. Mixed monolayer coverage on gold nanoparticles for interfacial stabilization of immiscible fluids. *Chem. Commun.* **2005**, 4050−4052.

(32) Ahn, Y.; Saha, J. K.; Schatz, G. C.; Jang, J. Molecular Dynamics Study of the Formation of a Self-Assembled Monolayer on Gold. *J. Phys. Chem. C* **2011**, *115*, 10668−10674.

(33) Ghorai, P. K.; Glotzer, S. C. Molecular dynamics simulation study of self-assembled monolayers of alkanethiol surfactants on spherical gold nanoparticles. *J. Phys. Chem. C* **2007**, *111*, 15857−15862.

(34) Zhao, X.; Leng, Y.; Cummings, P. T. Self-assembly of 1,4-benzenedithiolate/tetrahydrofuran on a gold surface: A Monte Carlo simulation study. *Langmuir* **2006**, *22*, 4116−4124.

(35) *Material Studio*, ver. 6.0; Accelrys Software Inc.: San Diego, CA, 2014.

(36) Chaban, V. Annealing relaxation of ultrasmall gold nanostructures. *Chem. Phys. Lett.* **2015**, *618*, 46−50.

(37) Andreeva, N. A.; Chaban, V. V. Global minimum search via annealing: Nanoscale gold clusters. *Chem. Phys. Lett.* **2015**, *622*, 75−79.

(38) Chaban, V. V. Systematic and efficient navigating potential energy surface: Data for silver doped gold clusters. *Data Brief* **2016**, *7*, 1321−1326.

(39) Joshi, K.; van Duin, A. C. T.; Jacob, T. Development of a ReaxFF description of gold oxides and initial application to cold welding of partially oxidized gold surfaces. *J. Mater. Chem.* **2010**, *20*, 10431−10437.

(40) Keith, J. A.; Fantauzzi, D.; Jacob, T.; van Duin, A. C. T. Reactive forcefield for simulating gold surfaces and nanoparticles. *Phys. Rev. B: Condens. Matter Mater. Phys.* **2010**, *81*, 235404.

(41) Jorgensen, W. L.; Madura, J. D.; Swenson, C. J. Optimized Intermolecular Potential Functions for Liquid Hydrocarbons. *J. Am. Chem. Soc.* **1984**, *106*, 6638−6646.

(42) Jorgensen, W. L.; Maxwell, D. S.; Tirado-Rives, J. Development and testing of the OPLS all-atom force field on conformational energetics and properties of organic liquids. *J. Am. Chem. Soc.* **1996**, *118*, 11225−11236.

(43) Plimpton, S. Fast Parallel Algorithms for Short-Range Molecular-Dynamics. *J. Comput. Phys.* **1995**, *117*, 1−19.

(44) Verlet, L. Computer "Experiments" on Classical Fluids. I. Thermodynamical Properties of Lennard-Jones Molecules. *Phys. Rev.* **1967**, *159*, 98−103.

(45) Luty, B. A.; Tironi, I. G.; van Gunsteren, W. F. Lattice-Sum Methods for Calculating Electrostatic Interactions in Molecular Simulations. *J. Chem. Phys.* **1995**, *103*, 3014−3021.

(46) Nosé, S. A unified formulation of the constant temperature molecular dynamics methods. *J. Chem. Phys.* **1984**, *81*, 511−519.

(47) Hoover, W. G. Canonical dynamics: Equilibrium phase-space distributions. *Phys. Rev. A* **1985**, *31*, 1695−1697.

(48) Parrinello, M.; Rahman, A. Polymorphic transitions in single crystals: A new molecular dynamics method. *J. Appl. Phys.* **1981**, *52*, 7182.

(49) Luedtke, W. D.; Landman, U. Structure and Thermodynamics of Self-Assembled Monolayers on Gold Nanocrystallites. *J. Phys. Chem. B* **1998**, *102*, 6566−6572.

(50) Luedtke, W. D.; Landman, U. Structure, Dynamics, and Thermodynamics of Passivated Gold Nanocrystallites and Their Assemblies. *J. Phys. Chem. B* **1996**, *100*, 13323−13329.

(51) Hostetler, M. J.; Wingate, J. E.; Zhong, C.-J.; Harris, J. E.; Vachet, R. W.; Clark, M. R.; Londono, J. D.; Green, S. J.; Stokes, J. J.; Wignall, G. D.; Glish, G. L.; Porter, M. D.; Evans, N. D.; Murray, R. W. Alkanethiolate gold cluster molecules with core diameters from 1.5 to 5.2 nm: Core and monolayer properties as a function of core size. *Langmuir* **1998**, *14*, 17−30.

(52) Jung, L. S.; Campbell, C. T. Sticking probabilities in adsorption of alkanethiols from liquid ethanol solution onto gold. *J. Phys. Chem. B* **2000**, *104*, 11168−11178.

(53) Jung, L. S.; Campbell, C. T. Sticking probabilities in adsorption from liquid solutions: Alkylthiols on gold. *Phys. Rev. Lett.* **2000**, *84*, 5164−5167.

(54) Fajín, J. L. C.; Teixeira, F.; Gomes, J. R. B.; Cordeiro, M. N. D. S. Effect of van der Waals interactions in the DFT description of self-assembled monolayers of thiols on gold. *Theor. Chem. Acc.* **2015**, *134*, 67.